



# Benefit of depolarization ratio at $\lambda = 1064$ nm for the retrieval of the aerosol microphysics from lidar measurements

J. Gasteiger and V. Freudenthaler

Meteorologisches Institut, Ludwig-Maximilians-Universität, Munich, Germany

Correspondence to: J. Gasteiger (josef.gasteiger@lmu.de)

Received: 17 April 2014 – Published in Atmos. Meas. Tech. Discuss.: 22 May 2014

Revised: 11 September 2014 – Accepted: 5 October 2014 – Published: 17 November 2014

**Abstract.** A better quantification of aerosol properties is required for improving the modelling of aerosol effects on weather and climate. This task is methodologically demanding due to the diversity of the microphysical properties of aerosols and the complex relation between their microphysical and optical properties. Advanced lidar systems provide spatially and temporally resolved information on the aerosol optical properties that is sufficient for the retrieval of important aerosol microphysical properties. Recently, the mass concentration of transported volcanic ash, which is relevant for the flight safety of aeroplanes, was retrieved from measurements of such lidar systems in southern Germany. The relative uncertainty of the retrieved mass concentration was on the order of  $\pm 50\%$ .

The present study investigates improvements of the retrieval accuracy when the capability of measuring the linear depolarization ratio at 1064 nm is added to the lidar setup. The lidar setups under investigation are based on those of MULIS and POLIS of the Ludwig-Maximilians-Universität in Munich (Germany) which measure the linear depolarization ratio at 355 and 532 nm with high accuracy. The improvements are determined by comparing uncertainties from retrievals applied to simulated measurements of this lidar setup with uncertainties obtained when the depolarization at 1064 nm is added to this setup. The simulated measurements are based on real lidar measurements of transported Eyjafjallajökull volcano ash. It is found that additional 1064 nm depolarization measurements significantly reduce the uncertainty of the retrieved mass concentration and effective particle size. This significant improvement in accuracy is the result of the increased sensitivity of the lidar setup to larger particles. The size dependence of the depolarization does not vary strongly with refractive index, thus we expect similar benefits for the retrieval in case of measurements of other

volcanic ash compositions and also for transported desert dust. For the retrieval of the single scattering albedo, which is relevant to the radiative transfer in aerosol layers, no significant improvements were found.

## 1 Introduction

The microphysical properties of aerosol particles are described by their size, shape, and composition. Knowledge of these properties is required, for example, in order to quantify the aerosol effect on the radiative transfer in weather and climate models; knowledge about aerosols, however, is still rather limited (e.g. Prather et al., 2008) and their effects are poorly quantified. Remote sensing is one of the most important tools used to increase knowledge of aerosols. For example, a sun photometer can measure the extinction of sun light by atmospheric constituents, and lidar systems emit very short laser pulses and detect with high temporal resolution the light that is backscattered by atmospheric constituents, allowing one to derive the backscatter coefficient  $\beta$  of the aerosols. When retrieving aerosol microphysical properties from measured optical remote sensing data, which is an inverse problem, the information content of the measurement data is often too limited for the retrieval of a unique solution. In the case of lidar, limitations arise from the small number of measured parameters and from the statistical and systematic uncertainties of the measurements. The result of a microphysical retrieval is usually a range of solutions with varying values for the microphysics that are compatible with the measurements within their uncertainties. While the calculation of the scattering properties of particles with known microphysics (the forward problem) is based on physical models, the examination of the range of solutions of an inverse

problem is based on the combination of physical models with mathematical search procedures (e.g. Twomey, 1977; Nakajima et al., 1983; Müller et al., 1999; Böckmann, 2001; Herman et al., 2008).

In recent decades, active remote sensing by lidar has become a powerful tool for aerosol research. Early lidar systems have been described for example by Collis (1966); and advanced methods and applications of the lidar technique have been presented by Weitkamp (2005). A major advantage of lidar among remote sensing techniques is that it is vertically resolving. Usually only cloud-free lidar data are used for aerosol research. In order to increase the information content of measurements, advanced aerosol lidars measure the backscatter coefficient,  $\beta$ , at different wavelengths, or use techniques that allow determination of the extinction coefficient,  $\alpha$ , of the aerosols (Raman lidar and high spectral resolution lidar; see Ansmann and Müller, 2005), and measure the polarization state of the backscattered light (Sassen, 2005). Most polarization lidars emit linearly polarized light and measure the fraction of the backscattered light that is polarized parallel to the polarization plane of the emitted laser light,  $I_{\parallel}$ , separately from the fraction that is polarized perpendicular to this plane,  $I_{\perp}$ . The linear volume depolarization ratio,  $\delta_1^v$ , (see, e.g. Freudenthaler et al., 2009) is the ratio:

$$\delta_1^v = \frac{I_{\perp}}{I_{\parallel}}. \quad (1)$$

Both air molecules and aerosol particles are relevant to the backscattering from the cloud-free atmosphere. The linear depolarization ratio,  $\delta_1$ , of the aerosol particles, which is of interest for aerosol characterization, can be extracted from  $\delta_1^v$  as shown by Biele et al. (2000). Observations of  $\delta_1$  allow one to distinguish spherical from non-spherical particles (Schotland et al., 1971) because  $\delta_1$  is zero for spherical particles and larger than zero for non-spherical particles. The depolarization parameter,  $d$ , as discussed by Gimmestad (2008), describes the same property as  $\delta_1$ , and a unique relationship exists between  $d$  and  $\delta_1$ :

$$d = \frac{2\delta_1}{1 + \delta_1}. \quad (2)$$

The circular depolarization ratio,  $\delta_c$ , is also uniquely related to  $\delta_1$ , if the assumption that particles and mirror particles are equiprobable and in random orientation is fulfilled, which is true for most practically important cases (Mishchenko and Hovenier, 1995), then:

$$\delta_c = \frac{2\delta_1}{1 - \delta_1}. \quad (3)$$

In the following we accept this assumption and thus  $\delta_1$ ,  $d$ , and  $\delta_c$  provide the same information about the aerosols, and the findings of our study employing  $\delta_1$  can be transferred to  $d$  and  $\delta_c$  as well.

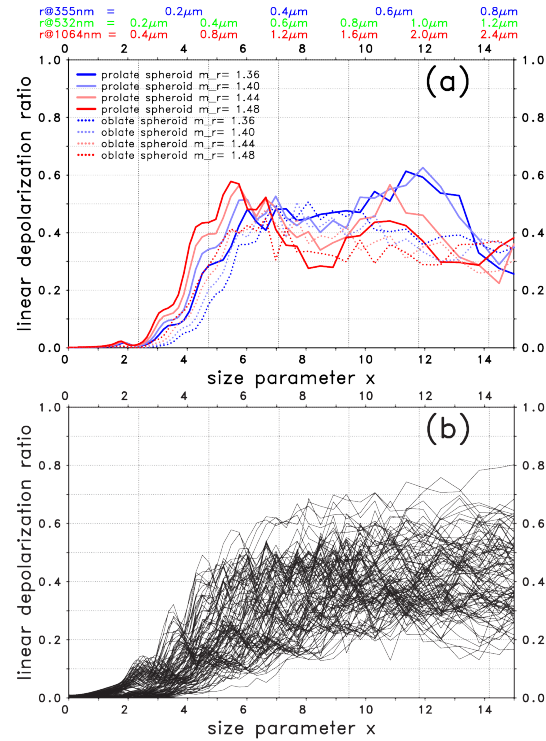


**Figure 1.** Linear depolarization ratio of non-absorbing oblate and prolate spheroids with  $m_r$  equal to 1.36, 1.40, 1.44, and 1.48 as a function of size parameter,  $x$ . The upper panel (**a**) considers only aspect ratio 1.6, whereas the lower panel (**b**) considers aspect ratios from 1.2 to 5.0; for reference, the corresponding particle radii for the lidar wavelengths are also given above the top axis.

Aside from providing the potential to detect spherical particles, the linear depolarization ratio,  $\delta_1$ , of non-spherical particles is also a function of the size parameter  $x = 2\pi r/\lambda$ , where  $r$  is the particle radius and  $\lambda$  the wavelength. As an example, the size parameter dependence is illustrated in Fig. 1a for non-absorbing oblate (dotted lines) and prolate (solid lines) spheroids with different real parts of the refractive index,  $m_r$ . The aspect ratio of the spheroids, which is defined as the ratio between the largest to the shortest axis, is set to 1.6. Additionally, the radii corresponding to the size parameter at the three main Nd:YAG laser wavelengths of lidars are shown above the top axis. Similar plots for further particle shapes are shown by Gasteiger et al. (2011b). Figure 1a shows that  $\delta_1$  is low for  $x \lesssim 2$  and high for  $x \gtrsim 6$ , with a transition region in between. The size parameters of  $x = 2$  and  $x = 6$  correspond to particle radii of about a third of the wavelength and about the same as the wavelength, respectively. Furthermore, the transition region is slightly shifted to lower size parameters as the real part of the refractive index increases. For oblate and prolate particles with aspect ratio 1.6,  $\delta_1$  is a strongly selective parameter regarding the particle size for particles with radii in the transition range. But if the measured  $\delta_1$  is high for all three Nd:YAG laser wavelengths, then we can

only conclude that the particle radii must be larger than about  $0.8 \mu\text{m}$ ; and if  $\delta_l$  is low for all wavelengths, then the particle radii must be smaller than about  $0.15 \mu\text{m}$ , or the particles are spheres. In general this characterization is also valid for spheroidal particles with a wide range of aspect ratios (see Fig. 1b), but with reduced selectivity in the transition range. Values for mixtures of spheroids are weighted means of the values for individual spheroids and are confined by the envelope of the cloud of curves. However, the linear depolarization ratio is only one of the parameters derived from lidar measurements, and the other parameters, i.e. the backscatter and extinction coefficients, show other dependencies on the size parameter and on the refractive index, which together improve the selectivity and enhance its range.

The combination of the advanced Raman lidar systems POLIS and MULIS (Freudenthaler et al., 2009) of the Meteorological Institute of the Ludwig-Maximilians-Universität in Munich, Germany, measures the linear depolarization ratio,  $\delta_l$ , and the extinction coefficient,  $\alpha$ , at two wavelengths:  $\lambda = 355$  and  $532 \text{ nm}$ ; and the backscatter coefficient,  $\beta$ , at three wavelengths:  $\lambda = 355, 532$ , and  $1064 \text{ nm}$ . Microphysical properties of transported volcanic ash were retrieved from measurements of this lidar setup on 17 April 2010 in Maisach (southern Germany) by means of comparisons between calculated optical properties of Monte Carlo sampled spheroid ensembles and optical properties from the measurements (Gasteiger et al., 2011a). Solutions are sampled ensembles with optical properties compatible with the measured properties. From the distribution of accepted solutions, relative uncertainties on the order of 50 % were found for the mass concentrations and effective radii of the ash particles; the main source of uncertainty was the low sensitivity of this lidar setup to the presence of large particles (about  $r > 3 \mu\text{m}$ ). Thus, enhancements of the existing lidar systems are envisaged in order to increase the accuracy of the retrieval. In order to support decisions on cost-effective enhancements of the lidar systems, the present contribution investigates to which extent channels for the linear depolarization ratio  $\delta_l$  at  $\lambda = 1064 \text{ nm}$ , abbreviated as  $\delta_{l,1064}$  in the following, can help to decrease the uncertainties associated with the microphysical retrieval. It is worth mentioning that channels for  $\delta_{l,1064}$  have already been integrated in a HSR lidar at the NASA Langley Research Center (Hair et al., 2008). In the present study, we compare retrieval results for simulated lidar measurements with different lidar setups (with and without channels for  $\delta_{l,1064}$ ). A single input ensemble is assumed in Sect. 3 to simulate the lidar measurements on which we apply the retrieval. In Sect. 4 the generality of the results from Sect. 3 is validated by considering a larger set of input ensembles used for simulating the lidar measurements.

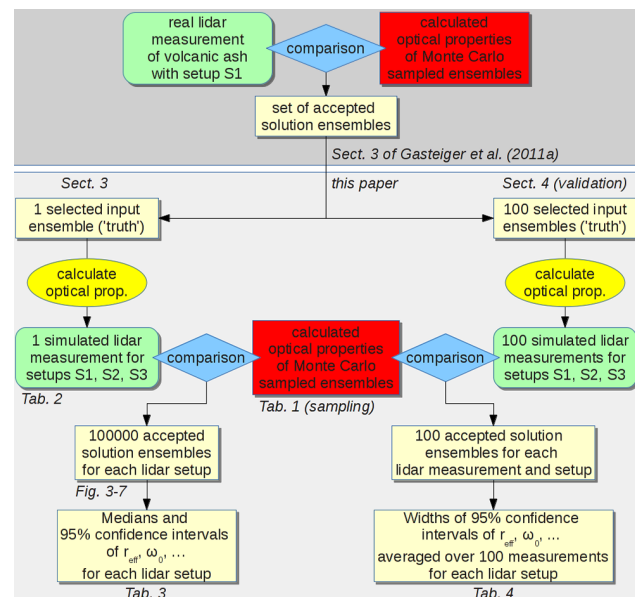


**Figure 2.** Investigation steps and their products in the current study.

## 2 Methods

Figure 2 shows the investigation steps of this study in a flow chart. The key components are the microphysical retrievals, represented by the combination of the green, blue, and red objects in Fig. 2. The retrieval approach is described in detail by an internal flow chart in Fig. 2 of Gasteiger et al. (2011a) and is briefly summarized here: the Monte Carlo method is applied for random sampling of the microphysical parameters of aerosol ensembles. The ensembles consist of oblate and prolate spheroids. The microphysics of the ensembles is described by parameters for the log-normal size distribution (modal radius  $r_0$ , width  $\sigma$ ), the relative frequency of prolate spheroids ( $\zeta$ , with  $1-\zeta$  being the relative frequency of oblate spheroids), the modified log-normal aspect ratio distributions (Eq. 16 of Gasteiger et al., 2011a) of oblate spheroids ( $\mu_o$  and  $\sigma_o$ ) and prolate spheroids ( $\mu_p$  and  $\sigma_p$ ), and the complex wavelength-independent refractive index (real part  $m_r$ , imaginary part  $m_i$ ). The ranges of microphysical parameters covered by the Monte Carlo sampling are given in Table 1. The integration limits are  $r_{\min} = 20 \text{ nm}$  to  $r_{\max} = 20 \mu\text{m}$ , and cross-section-equivalent radii are assumed. The particle mass density is assumed to be  $\rho = 2.6 \text{ g cm}^{-3}$  (adopted from mineral components of Hess et al., 1998). The optical properties of the sampled ensembles are calculated using the T-matrix method (Mishchenko and Travis, 1998). The geometric optics approach (Yang et al., 2007) is applied to large particles not covered by the T-matrix method. The radius coverage of the T-matrix method is illustrated in Fig. 4 of Wiegner et al. (2009) as a function of the aspect ratio for a refractive index close to 1.55: for example at  $\lambda = 532 \text{ nm}$ , the maximum radius of the T-matrix method is around  $r = 10 \mu\text{m}$  for prolate

**Table 1.** Ranges of microphysical parameters used for Monte Carlo sampling of the ensembles. Parameters include the modal radius,  $r_0$ , and the width of the log-normal size distribution,  $\sigma$ , the real,  $m_r$ , and imaginary,  $m_i$ , parts of the refractive index, the ratio of prolate spheroids to all spheroids,  $\zeta$ , parameters of modified log-normal aspect ratio distributions (Eq. 16 of Gasteiger et al., 2011a) for prolate spheroids ( $\mu_p$ ,  $\sigma_p$ ) and independent aspect ratio distribution parameters for oblate spheroids ( $\mu_o$ ,  $\sigma_o$ ).

Parameter	Range	
	lower bound	upper bound
$r_0$ (log sampling)	0.01 $\mu\text{m}$	10 $\mu\text{m}$
$\sigma$	1.2	4.0
$m_r$	1.28	2.00
$m_i$	0.0	0.1
$\zeta$	0	1
$\mu_p, \mu_o$	-0.6	0.6
$\sigma_p, \sigma_o$	0.5	1.5

spheroids with aspect ratio 1.6, but for aspect ratio 3.0 the geometric optics approach is required starting at  $r = 2.4 \mu\text{m}$ . The calculated optical properties of each sampled ensemble (red boxes in Fig. 2) are compared (blue hashes) with the real or simulated lidar measurements (green boxes), and those ensembles that are compatible with the measurements within the attributed uncertainty of the measurements are accepted as solutions of the retrieval. Finally, if the set of solutions is sufficiently large for statistical significance, the property of interest, e.g. the effective radius, is calculated for each ensemble in the set of solutions, and a distribution for the property of interest is obtained. Ranges including 95 % of the solutions, from 2.5 % to 97.5 % percentile, are denoted as (min .. max), which is the 95 % confidence interval. The widths of the 95 % confidence intervals are denoted as  ${}^{95\%} \Delta$  and provide an estimation of the uncertainties of the retrieved parameters.

To evaluate the benefit of the additional linear depolarization ratio,  $\delta_{l,1064}$ , we have to rely on simulated lidar measurements on which we apply the retrieval (Fig. 2). In order to make the simulated lidar measurements as realistic as possible with respect to relevant aerosol types, we select only input ensembles that are solutions for the retrieval from volcanic ash measurements in Maisach (Gasteiger et al., 2011a). We assume three different lidar setups: the first lidar setup (S1) is the lidar setup of MULIS and POLIS with the relative uncertainties obtained from volcanic ash measurements in Maisach; this setup does not include  $\delta_{l,1064}$ . The second (S2) and third (S3) setups include an additional channel for  $\delta_{l,1064}$ , but the other channels are the same as in setup S1. The second and third setups differ from each other by the relative uncertainty of  $\delta_{l,1064}$ : the third setup S3 assumes the relative uncertainty of  $\delta_{l,1064}$  to be the average of the relative uncertainties of  $\delta_l$  at 355 and 532 nm, whereas the uncertainty of  $\delta_{l,1064}$  in setup S2 is doubled compared with setup S3, in or-

der to investigate the effect of measurement uncertainties on the retrieval.

The present contribution focuses on the potential benefits of  $\delta_{l,1064}$  for the retrieval of the effective radius,  $r_{\text{eff}}$ , the mass-extinction conversion factor,  $\eta$ , and the single scattering albedo,  $\omega_0$ , which are calculated from the microphysical properties of the ensembles in the set of solutions. The effective radius  $r_{\text{eff}}$  (Hansen and Travis, 1974) is defined as

$$r_{\text{eff}} = \frac{\int r_c \cdot \pi r_c^2 n(r_c) dr_c}{\int \pi r_c^2 n(r_c) dr_c}, \quad (4)$$

where  $r_c$  is the cross-section-equivalent radius of the particles and  $n(r_c)$  the particle number density per radius interval. The effective radius,  $r_{\text{eff}}$ , is the cross-section-weighted average particle radius. Note that other definitions exist for the effective radius, see e.g. McFarquhar and Heymsfield (1998).

The mass-extinction conversion factor,  $\eta$  (unit:  $\text{g m}^{-2}$ ), is the ratio between the mass concentration,  $M$  (unit:  $\text{g m}^{-3}$ ), and the extinction coefficient,  $\alpha$  (unit:  $\text{m}^{-1}$ ):

$$\eta = \frac{M}{\alpha}. \quad (5)$$

$\eta$  is required for the conversion of extinction coefficients, as available from advanced lidar systems, to mass concentrations, e.g. of volcanic ash or cloud particles.

The single scattering albedo,  $\omega_0$ , is

$$\omega_0 = \frac{\alpha_{\text{sca}}}{\alpha}, \quad (6)$$

where  $\alpha_{\text{sca}}$  is the scattering coefficient and  $\alpha$  the extinction coefficient. Thus,  $\omega_0$  describes the ratio between the amount of light scattered by the particles and the amount of light interacting with the particles. Interacting light that is not scattered is absorbed by the particles and usually transformed into heat.  $\omega_0$  is an important parameter for the radiative transfer in aerosol layers.

### 3 Results

An input ensemble was randomly selected from the ensembles that are compatible with the lidar measurements of Eyjafjallajökull volcanic ash on the morning of 17 April 2010 at Maisach (Gasteiger et al., 2011a). This ensemble is referred to as the “truth” in this section and its calculated optical properties serve as input for the retrieval (see left branch of Fig. 2). The refractive index,  $m$ , is  $1.474 + 0.00705i$ , the modal radius of the log-normal size distribution,  $r_0$ , is  $0.516 \mu\text{m}$ , and its width,  $\sigma$ , is  $1.639$ . The effective radius,  $r_{\text{eff}}$ , of the input ensemble is  $0.95 \mu\text{m}$ . 71.05 % of the particles are prolate spheroids with a modified log-normal aspect ratio distribution with  $\mu_p = 0.234$  and  $\sigma_p = 1.253$ ; 28.95 % of the particles are oblate spheroids with aspect ratio distribution parameters  $\mu_o = 0.405$  and  $\sigma_o = 0.821$ . Table 2 summarizes

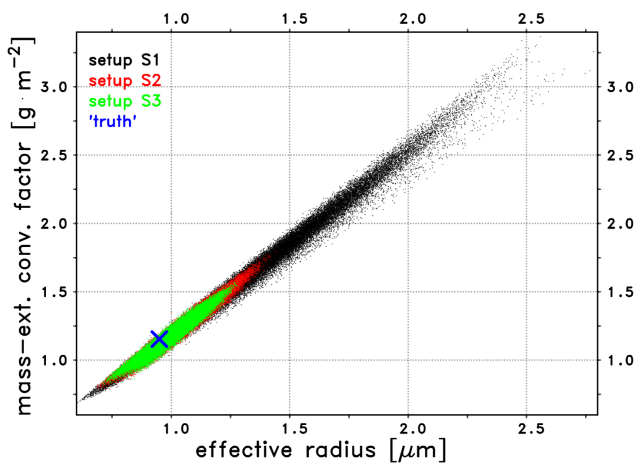


**Figure 3.** Mass-extinction conversion factor,  $\eta$ , at  $\lambda = 532$  nm as a function of effective radius,  $r_{\text{eff}}$ , of the solution ensembles for the three lidar setups. The properties of the input ensemble (“truth”) are denoted with a blue cross.

the relevant optical properties of this input ensemble. As we investigate only intensive properties, we scale the amount of particles such that the extinction coefficient  $\alpha$  has an arbitrary value of  $1 \text{ km}^{-1}$  at  $\lambda = 355$  nm.

All findings of the retrievals are compiled in Table 3. Figure 3 shows the mass-extinction conversion factors,  $\eta$ , of the retrieved solution ensembles as a function of their effective radii,  $r_{\text{eff}}$ . The black dots denote ensembles retrieved without consideration of  $\delta_{l,1064}$  (setup S1), the red and green dots show ensembles retrieved when  $\delta_{l,1064}$  is considered with different measurement uncertainties (setups S2 and S3). We retrieved 100 000 solution ensembles for each setup. The blue cross marks the properties of the ensemble used as input for the retrieval (“truth”). Analogous to the retrieval from the volcanic ash measurements presented by Gasteiger et al. (2011a), plotting  $\eta$  as a function of  $r_{\text{eff}}$  for the solutions leads to a distribution close to a straight line, indicating strong correlation between both ensemble parameters. The Pearson correlation coefficient between both parameters is 0.994 for setup S1. It is obvious from Fig. 3 that the uncertainty of the retrieved  $\eta$  and  $r_{\text{eff}}$  decreases notably if  $\delta_{l,1064}$  is considered. The 95 % confidence interval for  $r_{\text{eff}}$  is the range ( $0.78 \dots 2.03 \mu\text{m}$ ) with a width  $^{95\%} \Delta r_{\text{eff}} = 1.25 \mu\text{m}$  in case of non-consideration of  $\delta_{l,1064}$  (setup S1). When  $\delta_{l,1064}$  is considered with the higher uncertainty (setup S2), this range shrinks to ( $0.82 \dots 1.26 \mu\text{m}$ ) having a width  $^{95\%} \Delta r_{\text{eff}} = 0.44 \mu\text{m}$ . Thus,  $^{95\%} \Delta r_{\text{eff}}$  is reduced by a factor of 2.8 in setup S2 compared with setup S1. This reduction factor increases to 3.7, if the uncertainty of  $\delta_{l,1064}$  is reduced (setup S3). In accordance with the almost linear relationship between  $\eta$  and  $r_{\text{eff}}$ , the reduction factors for the  $\eta$  uncertainties are almost the same.

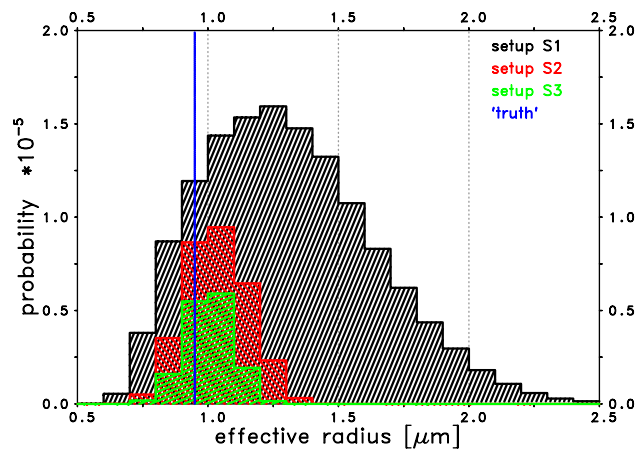


**Figure 4.** Probability distributions of solution ensembles for setups S1 (black), S2 (red), and S3 (green) with effective radius  $r_{\text{eff}}$  in bins of  $0.1 \mu\text{m}$  width;  $r_{\text{eff}}$  of the input ensemble (“truth”) is shown as a vertical line.

The probability for solution ensembles, i.e. the probability that a Monte Carlo-sampled ensemble is compatible with the measurements, is reduced by a factor of 4.3 (S2) and 8.9 (S3) when  $\delta_{l,1064}$  is added to the lidar setup. Figure 4 shows the probability for the three lidar setups that solution ensembles that fall within  $r_{\text{eff}}$  bins of  $0.1 \mu\text{m}$  width. The probability reduction in setups S2 and S3 happens due to  $\delta_{l,1064}$  serving as an additional criterion for the selection of the solution ensembles. The difference between the curves in Fig. 4 illustrates the effect of the consideration of  $\delta_{l,1064}$  on the retrieval of  $r_{\text{eff}}$ . It primarily sorts out ensembles with large  $r_{\text{eff}}$ , whereby ensembles with  $r_{\text{eff}} > 1.45 \mu\text{m}$  (S2) and  $r_{\text{eff}} > 1.31 \mu\text{m}$  (S3) do not occur anymore. Only about 28 % (S2) or 54 % (S3) of the ensembles are sorted out by the additional  $\delta_{l,1064}$  criterion if their  $r_{\text{eff}}$  is close to the  $r_{\text{eff}}$  of the truth ( $0.9 \dots 1.0 \mu\text{m}$ ).

Figures 5 and 6 show the real and imaginary parts of the refractive indices,  $m$ , versus the  $r_{\text{eff}}$  of the solution ensembles. By comparing the  $m-r_{\text{eff}}$  areas covered in the plots depending on the lidar setup it becomes clear that  $\delta_{l,1064}$  primarily helps to exclude ensembles with high  $r_{\text{eff}}$ . The uncertainty of the retrieved real part of the refractive index  $m_r$  is reduced by a factor of 1.4 (setup S2) and 1.5 (setup S3), while the uncertainty of  $m_i$  is reduced only by a factor of 1.21 and 1.25, respectively: this indicates slightly higher sensitivity of  $\delta_{l,1064}$  to the real part  $m_r$  than to the imaginary part  $m_i$ . This is consistent with the findings of Wiegner et al. (2009), where a higher sensitivity of  $\delta_l$  to changes of  $m_r$  than to changes of  $m_i$  was found for the shorter wavelength,  $\lambda = 532$  nm.

Figure 7 shows the probability for solution ensembles that fall within single scattering albedo,  $\omega_0$ , bins of 0.01 width at  $\lambda = 532$  nm. The consideration of  $\delta_{l,1064}$  removes a large fraction of ensembles with large  $\omega_0$  but, in general, it excludes ensembles throughout the whole range of  $\omega_0$  (compare red and green with black boxes). As a consequence,

**Table 2.** Simulated lidar-relevant optical properties and attributed uncertainties used as input (calculated from the “truth” ensemble) for the retrieval in Sect. 3; parameters are the extinction coefficient,  $\alpha$ , backscatter coefficient,  $\beta$ , and linear depolarization ratio,  $\delta_l$ , at different wavelengths; S1, S2, S3 denote the different lidar setups described in Sect. 2.

Parameter	Value	Relative uncertainty	Setup S1	Setup S2	Setup S3
$\alpha$ at 355 nm	$1.000 \text{ km}^{-1}$	$\pm 7.4 \%$	x	x	x
$\alpha$ at 532 nm	$1.0927 \text{ km}^{-1}$	$\pm 11.1 \%$	x	x	x
$\beta$ at 355 nm	$0.01908 \text{ km}^{-1} \text{ sr}^{-1}$	$\pm 5.3 \%$	x	x	x
$\beta$ at 532 nm	$0.02243 \text{ km}^{-1} \text{ sr}^{-1}$	$\pm 4.1 \%$	x	x	x
$\beta$ at 1064 nm	$0.01751 \text{ km}^{-1} \text{ sr}^{-1}$	$\pm 16.0 \%$	x	x	x
$\delta_l$ at 355 nm	0.3571	$\pm 4.4 \%$	x	x	x
$\delta_l$ at 532 nm	0.3687	$\pm 2.0 \%$	x	x	x
$\delta_l$ at 1064 nm	0.3005	$\pm 6.4 \%$		x	
$\delta_l$ at 1064 nm	0.3005	$\pm 3.2 \%$			x

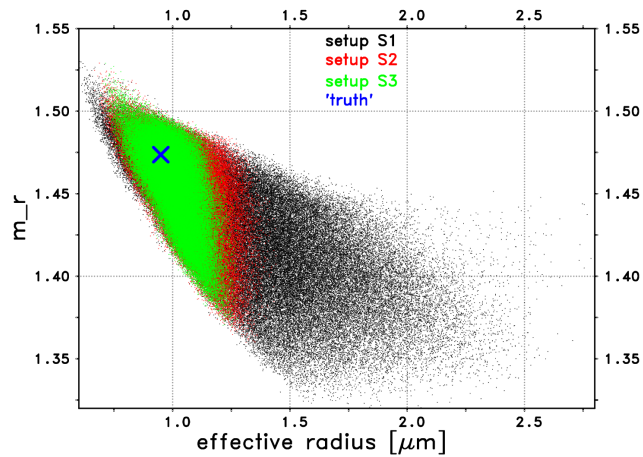


**Figure 5.** Real part of the refractive index,  $m_r$ , as a function of the effective radius,  $r_{\text{eff}}$ , of the solution ensembles for the three lidar setups. The properties of the input ensemble (“truth”) are denoted with a blue cross.

the uncertainty of the retrieved  $\omega_0$  is virtually independent of the lidar setup (reduction factors only about 1.06), which indicates that  $\delta_{l,1064}$  contains negligible information on  $\omega_0$ . This finding for  $\omega_0$  at  $\lambda = 532 \text{ nm}$  is also valid for  $\omega_0$  at  $\lambda = 1064 \text{ nm}$  (not shown).

#### 4 Statistical validation

Only a single randomly selected ensemble that is compatible with the volcanic ash measurements in Maisach (Gasteiger et al., 2011a) was used as input (“truth”) for the microphysical retrievals in the previous section. The question arises as to whether the above findings are specific for this single input ensemble or if they can be generalized to other input ensembles compatible with these volcanic ash measurements. In this section, we investigate retrievals for a larger set of input ensembles but with a smaller number of solution ensem-

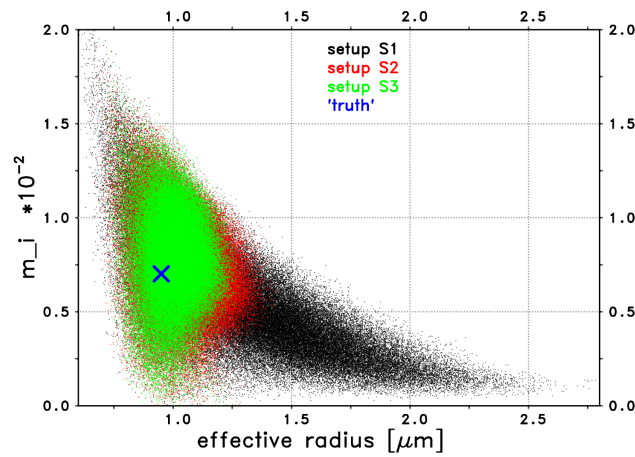


**Figure 6.** Imaginary part of the refractive index  $m_i$  as a function of the effective radius,  $r_{\text{eff}}$ , of the solution ensembles for the three lidar setups. The properties of the input ensemble (“truth”) are denoted with a blue cross.

bles (see right branch in Fig. 2). 100 randomly chosen input ensembles (“truth”) that are compatible with the volcanic ash measurements are used for this purpose, and, in order to save computation time, only 100 solution ensembles are retrieved for each combination of input ensemble and lidar setup. The effective radii of the 100 input ensembles cover the range from 0.70 to 2.05  $\mu\text{m}$ . The same lidar setups and relative uncertainties of the backscatter coefficients, extinction coefficients, and depolarization ratios are used as in the previous section (Table 2), and their values are simulated using the selected input ensembles. The  ${}^{95}\% \Delta$  widths of the retrieved parameters are calculated for each of the 100 input ensembles and three lidar setups, and average  ${}^{95}\% \Delta$  widths for each lidar setup are obtained by averaging over the 100 input ensembles.

Table 4 shows the average  ${}^{95}\% \Delta$  of the retrieved effective radius,  $r_{\text{eff}}$ , the mass-extinction conversion factor,  $\eta$ , and the single scattering albedo,  $\omega_0$ , for the three lidar setups. The

**Table 3.** Medians and 95 % confidence intervals (min .. max) of the effective radius,  $r_{\text{eff}}$ , the mass-extinction conversion factor,  $\eta$ , the single scattering albedo,  $\omega_0$ , and the refractive index,  $m$ , retrieved in Sect. 3 for the three lidar setups; for comparison the parameters of the input ensemble (“truth”) are also given; furthermore, the widths of the 95 % confidence intervals  ${}^{95\%}\Delta r_{\text{eff}}$ ,  ${}^{95\%}\Delta\eta$ , and  ${}^{95\%}\Delta\omega_0$  are given.

Parameter	Setup S1	Setup S2	Setup S3	“Truth”
$r_{\text{eff}}$ [μm]	1.28 (0.78 .. 2.03)	1.03 (0.82 .. 1.26)	1.01 (0.83 .. 1.17)	0.95
$\eta$ at 532 nm [ $\text{g m}^{-2}$ ]	1.55 (0.89 .. 2.56)	1.22 (0.94 .. 1.54)	1.19 (0.96 .. 1.42)	1.16
$\omega_0$ at 532 nm	0.896 (0.832 .. 0.958)	0.877 (0.827 .. 0.945)	0.875 (0.826 .. 0.945)	0.893
$m_r$	1.431 (1.355 .. 1.489)	1.457 (1.396 .. 1.492)	1.459 (1.404 .. 1.492)	1.474
$m_i \times 1000$	5.2 (1.3 .. 12.7)	7.6 (3.0 .. 12.4)	8.0 (3.1 .. 12.3)	7.0
${}^{95\%}\Delta r_{\text{eff}}$ [μm]	1.25	0.44	0.34	–
${}^{95\%}\Delta\eta$ at 532 nm [ $\text{g m}^{-2}$ ]	1.67	0.60	0.46	–
${}^{95\%}\Delta\omega_0$ at 532 nm	0.126	0.118	0.119	–

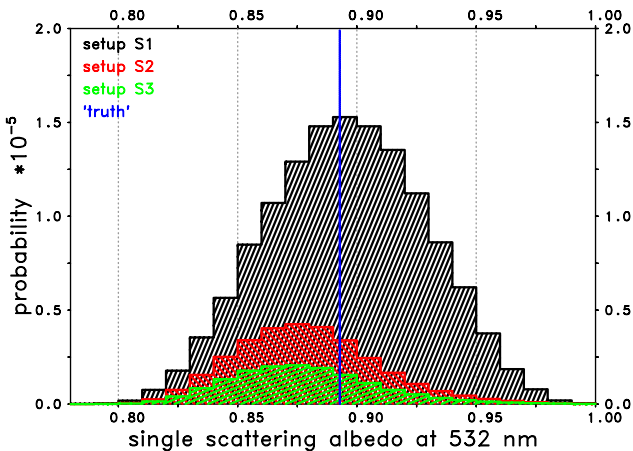


**Figure 7.** Probability distributions of solution ensembles for setups S1 (black), S2 (red), and S3 (green) with single scattering albedo,  $\omega_0$ , at  $\lambda = 532$  nm in bins of 0.01 width;  $\omega_0$  of the input ensemble (“truth”) is shown as a vertical line.

average  ${}^{95\%}\Delta r_{\text{eff}}$  and  ${}^{95\%}\Delta\eta$  is reduced by a factor of about 1.7 (setup S2) and 2.0 (setup S3) when  $\delta_{l,1064}$  is added to the lidar setup. By contrast, the average  ${}^{95\%}\Delta\omega_0$  at 532 nm is reduced only by a factor of about 1.1. Thus, the uncertainty of  $r_{\text{eff}}$  and  $\eta$  is reduced more significantly than the uncertainty of  $\omega_0$  by adding  $\delta_{l,1064}$  to the lidar setup. This qualitatively validates the generality of the findings from the previous section.

## 5 Conclusions

We evaluated the improvements that can be expected for the retrieval of microphysical properties of non-spherical aerosols by adding the capability of measuring the linear depolarization ratio at  $\lambda = 1064$  nm ( $\delta_{l,1064}$ ) to the lidar setup of MULIS and POLIS, which measure the linear depolarization ratio at 355 and 532 nm. We used simulated aerosol properties of transported volcanic ash ( $r_{\text{eff}} = 0.95$  μm) as input for

**Table 4.** Widths of the 95 % confidence intervals of the effective radius,  ${}^{95\%}\Delta r_{\text{eff}}$ , the mass-extinction conversion factor,  ${}^{95\%}\Delta\eta$ , and the single scattering albedo,  ${}^{95\%}\Delta\omega_0$ , averaged over 100 input ensembles (see Sect. 4 for details).

Parameter	Setup S1	Setup S2	Setup S3
${}^{95\%}\Delta r_{\text{eff}}$ [μm]	1.25	0.74	0.62
${}^{95\%}\Delta\eta$ at 532 nm [ $\text{g m}^{-2}$ ]	1.72	1.01	0.86
${}^{95\%}\Delta\omega_0$ at 532 nm	0.126	0.115	0.113

the retrievals assuming both this lidar setup and setups with additional  $\delta_{l,1064}$  capabilities. It was found that significant improvements can be expected for the retrieval of the effective radius,  $r_{\text{eff}}$ , and the mass-extinction conversion factor,  $\eta$ , whereas no significant improvement should be expected for the retrieval of the single scattering albedo,  $\omega_0$ . A statistical analysis using retrievals with lower sampling statistics applied to a set of 100 different simulated measurements generalizes the above-mentioned improvements for a bigger ensemble of volcanic ash properties. The significant improvements for  $r_{\text{eff}}$  and  $\eta$  are primarily a result of the sensitivity of  $\delta_{l,1064}$  to the presence of larger particles. These improvements are found even if the uncertainty of the  $\delta_l$  measurements at 1064 nm is slightly higher than the uncertainty of the  $\delta_l$  measurements at 355 and 532 nm.

Although in the present study wavelength independence of the refractive index was assumed, it needs to be emphasized that the refractive index of real aerosol particles can be wavelength-dependent and vary between the particles of an ensemble (e.g. Schumann et al., 2011). Measurements of the refractive index of mineral and volcanic particles suggest only weak spectral variation of the real part in the wavelength range of our lidars (355 to 1064 nm), whereas the imaginary part can vary considerably in this spectral range (see for example Wagner et al., 2012, and references therein). The effects of the refractive index assumption on the retrieval results will be analysed in future studies.

Our case study was conducted using ash compositions of the input ensembles, which are compatible with our lidar measurements of transported Eyjafjallajökull ash. Figure 1a shows that a variability of the refractive index leads only to a small variability of the size parameter of the transition region between low and high  $\delta_l$ . Hence our results for this specific volcano ash are transferable to ashes from other volcanoes with other refractive indices too. However, the real part of the refractive indices,  $m_r$ , retrieved with our methodology is smaller than  $m_r$  determined with other approaches (e.g. Schumann et al., 2011). This difference has to be investigated in future.

Benefits for the retrieval of the effective radius and mass concentration can be expected from  $\delta_{l,1064}$  data also in case of transported mineral dust, which is comparable to transported volcanic ash with respect to most relevant properties, like the particle size range, the composition of minerals and rocks, and high  $\delta_l$  values (Langmann, 2013; Groß et al., 2012). The retrieval uncertainty probably gets too high for useful  $r_{\text{eff}}$  and  $\eta$  retrievals in the case of measurements very close to the aerosol source, where  $r_{\text{eff}}$  of the particles can be considerably larger than the longest wavelength used. The benefits of  $\delta_{l,1064}$  are expected to be qualitatively similar for other advanced lidar systems that operate within or close to the visible spectral range. Even for simple lidar systems, such as ceilometers (Wiegner et al., 2014), the capability of measuring  $\delta_{l,1064}$  would be quite a useful enhancement because of its sensitivity to large non-spherical particles, such as desert dust and volcanic ash aerosols.

In summary, we have shown that the channel for the linear depolarization ratio  $\delta_l$  at  $\lambda = 1064$  nm is a valuable extension to existing lidar systems for the retrieval of the effective particle size and the mass concentration of transported volcanic ash. We expect the benefits to be comparable in cases of other non-spherical aerosol types with similar  $r_{\text{eff}}$ .

**Acknowledgements.** This work was partly funded by the LMUexcellent project EVAAeNT. We thank the reviewers for valuable comments helping us to improve the paper.

Edited by: U. Wandinger

## References

- Ansmann, A. and Müller, D.: Lidar and Atmospheric Aerosol Particles, in: Lidar, edited by: Weitkamp, C., Vol. 102 of Springer Series in Optical Sciences, 105–141, Springer New York, doi:10.1007/0-387-25101-4\_4, 2005.
- Biele, J., Beyerle, G., and Baumgarten, G.: Polarization Lidar: Correction of instrumental effects, Opt. Express, 7, 427–435, doi:10.1364/OE.7.000427, 2000.
- Böckmann, C.: Hybrid regularization method for the ill-posed inversion of multiwavelength lidar data in the retrieval of aerosol size distributions, Appl. Optics, 40, 1329–1342, doi:10.1364/AO.40.001329, 2001.
- Collis, R. T. H.: Lidar: A new atmospheric probe, Q. J. Roy. Meteorol. Soc., 92, 220–230, doi:10.1002/qj.49709239205, 1966.
- Freudenthaler, V., Esselborn, M., Wiegner, M., Heese, B., Tesche, M., Ansmann, A., Müller, D., Althausen, D., Wirth, M., Fix, A., Ehret, G., Knippertz, P., Toledano, C., Gasteiger, J., Garhammer, M., and Seefeldner, M.: Depolarization ratio profiling at several wavelengths in pure Saharan dust during SAMUM 2006, Tellus B, 61, 165–179, doi:10.1111/j.1600-0889.2008.00396.x, 2009.
- Gasteiger, J., Groß, S., Freudenthaler, V., and Wiegner, M.: Volcanic ash from Iceland over Munich: mass concentration retrieved from ground-based remote sensing measurements, Atmos. Chem. Phys., 11, 2209–2223, doi:10.5194/acp-11-2209-2011, 2011a.
- Gasteiger, J., Wiegner, M., Groß, S., Freudenthaler, V., Toledano, C., Tesche, M., and Kandler, K.: Modeling lidar-relevant optical properties of complex mineral dust aerosols, Tellus B, 63, 725–741, doi:10.1111/j.1600-0889.2011.00559.x, 2011b.
- Gimmemstad, G. G.: Reexamination of depolarization in lidar measurements, Appl. Optics, 47, 3795–3802, doi:10.1364/AO.47.003795, 2008.
- Groß, S., Freudenthaler, V., Wiegner, M., Gasteiger, J., Geiß, A., and Schnell, F.: Dual-wavelength linear depolarization ratio of volcanic aerosols: lidar measurements of the Eyjafjallajökull plume over Maisach, Germany, Atmos. Environ., 48, 85–96, doi:10.1016/j.atmosenv.2011.06.017, 2012.
- Hair, J. W., Hostetler, C. A., Cook, A. L., Harper, D. B., Ferrare, R. A., Mack, T. L., Welch, W., Izquierdo, L. R., and Hovis, F. E.: Airborne High Spectral Resolution Lidar for profiling aerosol optical properties, Appl. Optics, 47, 6734–6752, doi:10.1364/AO.47.006734, 2008.
- Hansen, J. E. and Travis, L. D.: Light scattering in planetary atmospheres, Space Sci. Rev., 16, 527–610, doi:10.1007/BF00168069, 1974.
- Herman, B. R., Gross, B., Moshary, F., and Ahmed, S.: Bayesian assessment of uncertainty in aerosol size distributions and index of refraction retrieved from multiwavelength lidar measurements, Appl. Optics, 47, 1617–1627, doi:10.1364/AO.47.001617, 2008.
- Hess, M., Koepke, P., and Schult, I.: Optical Properties of Aerosols and Clouds: The Software Package OPAC, B. Am. Meteorol. Soc., 79, 831–844, doi:10.1175/1520-0477(1998)079<0831:OPOAAC>2.0.CO;2, 1998.
- Langmann, B.: Volcanic Ash versus Mineral Dust: Atmospheric Processing and Environmental and Climate Impacts, ISRN Atmospheric Sciences, 2013, ID 245076, doi:10.1155/2013/245076, 2013.
- McFarquhar, G. M. and Heymsfield, A. J.: The Definition and Significance of an Effective Radius for Ice Clouds, J. Atmos. Sci., 55, 2039–2052, doi:10.1175/1520-0469(1998)055<2039:TDASOA>2.0.CO;2, 1998.
- Mishchenko, M. I. and Hovenier, J. W.: Depolarization of light backscattered by randomly oriented nonspherical particles, Opt. Lett., 20, 1356–1358, doi:10.1364/OL.20.001356, 1995.
- Mishchenko, M. I. and Travis, L. D.: Capabilities and limitations of a current Fortran implementation of the T-Matrix method for randomly oriented, rotationally symmetric scatterers, J. Quant. Spectrosc. Ra., 60, 309–324, doi:10.1016/S0022-4073(98)00008-9, 1998.
- Müller, D., Wandinger, U., and Ansmann, A.: Microphysical Particle Parameters from Extinction and Backscatter Lidar Data

- by Inversion with Regularization: Theory, *Appl. Optics*, 38, 2346–2357, doi:10.1364/AO.38.002346, 1999.
- Nakajima, T., Tanaka, M., and Yamauchi, T.: Retrieval of the optical properties of aerosols from aureole and extinction data, *Appl. Optics*, 22, 2951–2959, doi:10.1364/AO.22.002951, 1983.
- Prather, K. A., Hatch, C. D., and Grassian, V. H.: Analysis of Atmospheric Aerosols, *Annu. Rev. Anal. Chem.*, 1, 485–514, doi:10.1146/annurev.anchem.1.031207.113030, 2008.
- Sassen, K.: Polarization in Lidar, in: *Lidar*, edited by: Weitkamp, C., Vol. 102 of Springer Series in Optical Sciences, 19–42, Springer New York, doi:10.1007/0-387-25101-4\_2, 2005.
- Schotland, R. M., Sassen, K., and Stone, R.: Observations by Lidar of Linear Depolarization Ratios for Hydrometeors, *J. Appl. Meteorol.*, 10, 1011–1017, doi:10.1175/1520-0450(1971)010<1011:OBLOLD>2.0.CO;2, 1971.
- Schumann, U., Weinzierl, B., Reitebuch, O., Schlager, H., Minikin, A., Forster, C., Baumann, R., Sailer, T., Graf, K., Mannstein, H., Voigt, C., Rahm, S., Simmet, R., Scheibe, M., Lichtenstern, M., Stock, P., Rüba, H., Schäuble, D., Tafferner, A., Rautenhaus, M., Gerz, T., Ziereis, H., Krautstrunk, M., Mallaun, C., Gayet, J.-F., Lieke, K., Kandler, K., Ebert, M., Weinbruch, S., Stohl, A., Gasteiger, J., Groß, S., Freudenthaler, V., Wiegner, M., Ansmann, A., Tesche, M., Olafsson, H., and Sturm, K.: Airborne observations of the Eyjafjallajökull volcano ash cloud over Europe during air space closure in April and May 2010, *Atmos. Chem. Phys.*, 11, 2245–2279, doi:10.5194/acp-11-2245-2011, 2011.
- Twomey, S.: *Introduction to the Mathematics of Inversion in Remote Sensing and Indirect Measurements*, Dover Publications, Mineola, New York, 1977.
- Wagner, R., Ajtai, T., Kandler, K., Lieke, K., Linke, C., Müller, T., Schnaiter, M., and Vragel, M.: Complex refractive indices of Saharan dust samples at visible and near UV wavelengths: a laboratory study, *Atmos. Chem. Phys.*, 12, 2491–2512, doi:10.5194/acp-12-2491-2012, 2012.
- Weitkamp, C. (Ed.): *LIDAR: Range-Resolved Optical Remote Sensing of the Atmosphere*, Springer, doi:10.1007/0-387-25101-4, 2005.
- Wiegner, M., Gasteiger, J., Kandler, K., Weinzierl, B., Rasp, K., Eselborn, M., Freudenthaler, V., Heese, B., Toledano, C., Tesche, M., and Althausen, D.: Numerical simulations of optical properties of Saharan dust aerosols with emphasis on lidar applications, *Tellus B*, 61, 180–194, doi:10.1111/j.1600-0889.2008.00381.x, 2009.
- Wiegner, M., Madonna, F., Binietoglu, I., Forkel, R., Gasteiger, J., Geiß, A., Pappalardo, G., Schäfer, K., and Thomas, W.: What is the benefit of ceilometers for aerosol remote sensing? An answer from EARLINET, *Atmos. Meas. Tech.*, 7, 1979–1997, doi:10.5194/amt-7-1979-2014, 2014.
- Yang, P., Feng, Q., Hong, G., Kattawar, G. W., Wiscombe, W. J., Mishchenko, M. I., Dubovik, O., Laszlo, I., and Sokolik, I. N.: Modeling of the scattering and radiative properties of non-spherical dust-like aerosols, *J. Aerosol Sci.*, 38, 995–1014, doi:10.1016/j.jaerosci.2007.07.001, 2007.